Defocus Corrected Large Area Cryo-EM (DeCo-LACE) for Label-Free Detection of Molecules across Entire Cell Sections

Authors

- **Johannes Elferich** ✉ 0000-0002-9911-706X

  RNA Therapeutics Institute, University of Massachusetts Chan Medical School, Worcester, MA, USA; Howard Hughes Medical Institute, USA

- **Giulia Schiroli** 0000-0002-9812-8728

  Center for Regenerative Medicine, Massachusetts General Hospital, Boston, MA, USA; Harvard Stem Cell Institute, Cambridge, MA, USA; Department of Stem Cell and Regenerative Biology, Harvard University, Cambridge, MA, USA

- **David Scadden** 0000-0001-9821-7133

  Center for Regenerative Medicine, Massachusetts General Hospital, Boston, MA, USA; Harvard Stem Cell Institute, Cambridge, MA, USA; Department of Stem Cell and Regenerative Biology, Harvard University, Cambridge, MA, USA

- **Nikolaus Grigorieff** ✉ 0000-0002-1506-909X

  RNA Therapeutics Institute, University of Massachusetts Chan Medical School, Worcester, MA, USA; Howard Hughes Medical Institute, USA

✉ — correspondence preferred via GitHub Issues. Otherwise, address correspondence to johannes.elferich@umassmed.edu and niko@grigorieff.org.

Abstract

A major goal of biological imaging is localization of biomolecules inside a cell. Fluorescence microscopy can localize biomolecules inside whole cells and tissues, but its ability to count biomolecules and accuracy of the spatial

coordinates is limited by the wavelength of visible light. Cryo-electron microscopy (cryo-EM) provides highly accurate position and orientation information of biomolecules but is often confined to small fields of view inside a cell, limiting biological context. In this study we use a new data-acquisition scheme called "Defocus-Corrected Large-Area cryo-EM" (DeCo-LACE) to collect high-resolution images of entire sections (100 – 200 nm thick lamellae) of neutrophil-like mouse cells, representing 1-2% of the total cellular volume. We use 2D template matching (2DTM) to determine localization and orientation of the large ribosomal subunit in these sections. These data provide "maps" of ribosomes across entire sections of mammalian cells. This high-throughput cryo-EM data collection approach together with 2DTM will advance visual proteomics and provide biological insight that cannot be obtained by other methods.

Introduction

A major goal in understanding cellular processes is the knowledge of the amounts, location, interactions, and conformations of biomolecules inside the cell. This knowledge can be obtained by approaches broadly divided into label- and label-free techniques. In label-dependent techniques a probe is physically attached to a molecule of interest that is able to be detected by its strong signal, such as a fluorescent molecule. In label-free techniques, the physical properties of molecules themselves are used for detection. An example for this is proteomics using mass-spectrometry [1]. The advantage of label-free techniques is that they can provide information over thousands of molecules, while label-dependent techniques offer highly specific information for a few molecules. in particular, spatial information is primarily achieved using label-dependent techniques, such as fluorescence microscopy [2].

Cryo-electron microscopy (cryo-EM) has the potential to directly visualize the arrangement of atoms that compose biomolecules inside of cells, thereby allowing label-free detection with high spatial accuracy. This has been called "visual proteomics" [3]. Since cryo-EM requires thin samples (<500nm), imaging of biomolecules inside cells is restricted to small organisms, thin regions of cells, or samples that have been suitably thinned. Thinning can be achieved either by mechanical sectioning [4] or by milling using a focused ion beam (FIB) [5]. This complex workflow leads to a low throughput of cryo-EM imaging of cells and is further limited by the fact that at the required magnifications, typical fields of view (FOV) are very small compared to mammalian cells, and the FOV achieved by label-dependent techniques such as fluorescence light microscopy. The predominant cryo-EM technique for the localization of biomolecules of defined size and shape inside cells is cryo-electron tomography [6]. However, the requirement of a tilt series at every imaged location and subsequent image alignment, severely limits the throughput for molecular localization.

An alternative approach is to identify molecules by their structural "fingerprint" in single projection using "2D template-matching" (2DTM) [7,8,9]. In this method, a 3D model of a biomolecule is used as a template to find 2D projections that match the molecules visible in the electron micrographs. This method requires a projection search

on a fine angular grid, and the projections are used to find local cross-correlation peaks with the micrograph. Since the location of a biomolecule in the z-direction causes predictable aberrations to the projection image, this method can be used to calculate complete 3D coordinates and orientations of a biomolecule in a cellular sample [8].

Here we apply 2DTM of the ribosome large subunit (LSU) to a conditionally immortalized *mus musculus* (mouse) cell line that gives rise to functional mature neutrophils [10]. We chose these cells because genetic defects in the ribosome machinery often leads to hematopoietic disease [11] and direct quantification of ribosome location, number and conformational states in hematopoietic cells could lead to new insight into hematopoietic disease [12]. To increase the amount of collected data and to provide unbiased sampling of the whole lamella, we devised a new data-acquisition scheme, "Defocus-Corrected Large Area Cryo-Electron microscopy" (DeCo-LACE). 2DTM allows us to test whether aberrations caused by large beam-image shifts and highly condensed beams deteriorate the high-resolution signal. We find that these aberrations do not impede LSU detection by 2DTM. The resulting data provide a description of ribosome distribution in an entire lamella, which represent 1-2% of the cellular volume. We find a highly heterogeneous density of ribosomes within the cell. Analysis of the throughput in this method suggests that for the foreseeable future computation will be the bottleneck for visual proteomics.

Results

2DTM detects large ribosomal subunits in cryo-FIB lamellae of mammalian cells

FIB-milled *Saccharomyces cerevisiae* (yeast) cells are sufficiently well preserved to permit localization of 60S ribosomal subunits with 2DTM [13]. Due to the larger size of mammalian cells compared to yeast cells, it was unclear whether plunge freezing would be adequate to produce vitreous ice across the whole volume of the cell. To test this we prepared cryo-lamellae of mouse neutrophil cells. A low magnification image of a representative lamella clearly shows cellular features consistent with a neutrophile-like phenotype, mainly a segmented nucleus and a plethora of membrane-organelles, corresponding to the granules and secretory vesicles of neutrophils (Fig. [1]A). We then proceeded to acquire micrographs on this lamella with a defocus of 0.5-1.0 µm, 30 $e^-/Å^2/s$ exposure and 1.76 Å pixel size. We manually selected multiple locations in the lamella and acquired micrographs using standard low-dose techniques where focusing is performed on a sacrificial area. The resulting micrographs showed smooth bilayered membranes and no signs of crystalline ice (Fig. [1]C,D), indicating successful vitrification throughout the lamella.

We used an atomic model of the 60S mouse ribosomal subunit (6SWA) for 2DTM [14]. In a subset of images, the distribution of cross-correlation scores significantly exceeded the distribution expected from images devoid of detectable targets. In the resulting scaled maximum-intensity projections (MIPs), clear peaks with SNR values up to 10 were apparent (Fig. [2 - figure supplement 1]A). Using a threshold criterion to select significant targets (see Methods), we found that in images of cytosolic compartments there were 10-500 ribosomes within one micrograph

(Fig. [1]B-E). Notably, we found no targets in areas corresponding to the nucleus (Fig. [1]B) or mitochondria (Fig. 1D). In the cytoplasm, we found a highly variable number of targets, only ~ 50 in some exposures (Fig. [1]E) and up to 500 in others (Fig. [1]C). However, it is unclear whether this ten-fold difference in local ribosome concentration is due to technical variation, such as sample thickness, or biological variation. To differentiate between the two we reasoned it was important to not manually choose imaging regions and to collect larger amounts of data. We therefore set out to collect cryo-EM data for 2DTM from mammalian cell lamellae in a high-throughput unbiased fashion.

DeCo-LACE for 2D imaging of whole lamellae

In order to obtain high-resolution data from complete lamellae, we developed a new approach for data collection. This approach uses three key strategies: (1) every electron that exposes a fresh area of the sample is collected on the camera (2) image shift is used to precisely and quickly raster the surface of a lamella and (3) focusing is done without using a sacrificial area (Fig. [2]A).

To ensure that every electron exposing a fresh area of the sample is captured by the detector, we adjusted the electron beam size to be entirely contained by the detector area. During canonical low-dose imaging, the microscope is configured so that the focal plane is identical to the eucentric plane of the specimen stage. This leaves the C2 aperture out of focus, resulting in ripples at the edge of the beam (Fig. [2]D). While these ripples are low-resolution features that likely do not interfere with 2DTM [7], we also tested data collection under conditions where the C2 aperture is in focus ("fringe-free", Fig. [2]E) [15].

We then centered a lamella on the optical axis of the microscope and used the image shift controls of the microscope to systematically scan the whole surface of the lamella in a hexagonal pattern (Fig. [2]A,C). Instead of focusing on a sacrificial area, we determined the defocus from every exposure after it was taken. The defocus was then adjusted based on the difference between desired and measured defocus (Fig. [2]B). Since we used a serpentine pattern for data collection, every exposure was close to the previous exposure, making large changes in the defocus unlikely. Furthermore, we started our acquisition pattern on the platinum deposition edge to make sure that the initial exposure where the defocus was not yet adjusted did not contain any biologically relevant information.

We used this strategy to collect data on eight lamellae, four using the eucentric focus condition, hereafter referred to as Lamella$_{EUC}$, and four using the fringe-free condition, hereafter referred to as Lamella$_{FFF}$ (Fig. [3] A+D, Fig. [4 - figure supplement 4]A). We were able to collect data with a highly consistent defocus of 800 nm (Fig. [2]F), both in the eucentric focus and fringe-free focus condition. To ensure that data were collected consistently, we mapped defocus values as a function of the applied image shift (Fig. [3 - figure supplement 1]A). This demonstrated that the defocus was consistent across a lamella, except for rare outliers and in images containing contamination. We also plotted the measured objective astigmatism of each lamella and found that it varies with the applied image

shift, becoming more astigmatic mostly due to image shift in the x direction (Fig. [3 - figure supplement 1]B). While approaches exist to correct for this during the data collection [16], we opted to not use these approaches in our initial experiments. We reasoned that because 2DTM depends on high-resolution information, this would be an excellent test of how much these aberration affect imaging.

We assembled the tile micrographs into a montage using the image-shift values and the SerialEM calibration followed by cross-correlation based refinement (see Methods). In the resulting montages, the same cellular features visible in the overview images are apparent (Fig. [3]B+E, Fig. [4 - figure supplement 4]B), however due to the high magnification and low defocus many more details, such as the membrane bilayer separation, can be observed (Fig. [3]C+F). For montages collected using the eucentric condition, there are clearly visible fringes at the edges between the tiles (Fig. [3]C), which are absent in the fringe-free focus montages (Fig. [3]F). In our analysis below, we show that these fringes do not impede target detection by 2DTM, making them primarily an aesthetic issue. We also note that the tiling pattern is visible in the montages (Fig. [3]B+E), which we believe is due to the non-linear behavior of the K3 camera since we can observe these shading artifacts in micrographs of a condensed beam over vacuum (Fig. [4 - figure supplement 3]).

The montages show membrane vesicles and granules with highly variable sizes and density. We found that a substantial number of granules, which are characterized by higher density inside the the surrounding cytosol [17], seemed to contain a membrane-enclosed inclusion with density similar to the surrounding cytosol (Fig. [4 - figure supplement 4]C) and could therefore be formed by inward budding of the granule membrane. These granules were 150-300 nm in diameter and the inclusions were 100-200 nm in diameter. Based on these dimensions the granules are either azurophil or specific granules [17]. To our knowledge, these inclusion have not been described in granulocytes and are further described and discussed below.

2DTM of DeCo-LACE data reveals large ribosomal subunit distribution in cellular cross-sections

In our initial attempts of using 2DTM on micrographs acquired with the DeCo-LACE protocol, we did not observe any SNR peaks above threshold using the large subunit of the mouse ribosome (Fig. [4 - figure supplement 1]A). We reasoned that the edges of the beam might interfere with motion-correction of the movies as they represent strong low-resolution features that do not move with the sample. When we cropped the movie frames to exclude the beam edges, the estimated amount of motion increased (Fig. [4 - figure supplement 1]B), consistent with successful tracking of sample motion. Furthermore, in the motion-corrected average we could identify significant SNR peaks (Fig. [4 - figure supplement 1]B), confirming the high sensitivity of 2DTM to the presence of high-resolution signal preserved in the images by the motion correction. To streamline data processing, we implemented a function in unblur to consider only a defined central area of a movie for estimation of sample motion, while still averaging the complete movie frames (Fig. [4 - figure supplement 1]C). Using this approach, we motion-corrected all tiles in the

eight lamellae and found consistently total motion below 1 Å per frame (Fig. [4 - figure supplement 2] A). In some lamellae we found increased motion in the lamella center, which indicates areas of variable mechanical stability within FIB-milled lamellae. In some micrographs we also observed that the beam edges gave rise to artifacts in the MIP and numerous false-positive detections at the edge of the illuminated area (Fig. [4 - figure supplement 1]D). A similar phenomenon was observed on isolated "hot" pixels in unilluminated areas. To overcome this issue we implemented a function in unblur to replace dark areas in the micrograph with Gaussian noise (see Methods), with mean and standard deviation matching the illuminated portion of the micrograph (Fig. [4 - figure supplement 1]D+E). Together, these pre-processing steps enabled us to perform 2DTM on all tiles of the eight lamellae.

We used the tile positions to calculate the positions of the detected LSUs in the lamellae (Fig. [4]A, Fig. [5]A, Movie 1, Movie 2). Overlaying these positions of the lamellae montages reveals LSU distribution throughout the FIB-milled slices of individual cells. Consistent with prior observations imaging selected views in yeast [13], organelles like the nucleus and mitochondria only showed sporadic targets detected with low SNRs, consistent with the estimated false-positive rate of one per tile. For each detected target we also calculated the Z positions from the individual estimated defocus and defocus offset for each tile. When viewed from the side, the ribosome positions therefore show the slight tilts of the lamellae relative to the microscope frame of reference (Fig. [4]B, Fig. [5]B, Movie 1, Movie 2). Furthermore, the side views indicated that lamellae were thinner at the leading edge. Indeed, when plotting the transmitted beam intensities in individual tiles as a function of beam image-shift, we observed substantially higher intensities at the leading edge (Fig. [4 - figure supplement 2]B), which in energy-filtered TEM indicates a thinner sample [18]. Even though we prepared the lamellae with the "overtilt" approach [19], this means that LSU densities across the lamellae can be skewed by a change in thickness, and better sample preparation methods are needed to generate more even samples.

As described in [7] the 2DTM SNR threshold for detecting a target is chosen to result in one false positive detection per image searched. We would therefore expect to find one false positive detection per tile. We reasoned that the large nuclear area imaged by DeCo-LACE could be used to test whether this assumption is true. In the 670 tiles containing exclusively nucleus (as manually annotated from the overview image) we detected 247 targets, making the false-positive rate more than twofold lower than expected. Since earlier work shows that 2DTM with the LSU can produce matches to nuclear ribosome biogenesis intermediates [13], this could even be an overestimate of the false-positive rate. This suggests that the detection threshold could be even lower, which is an area of ongoing research.

Close inspection of the LSU positions in the lamellae revealed several interesting features. LSUs could be seen associating with membranes, in patterns reminiscent of the rough endoplasmic reticulum (Fig. [4]C, Fig. [5]C) or the outer nuclear membrane (Fig. [4]D). We also observed LSUs forming ring-like structures (Fig. [4]E), potentially indicating circularized mRNAs [20]. While ribosomes were for the most part excluded from the numerous gran-

ules observed in the cytoplasm, in some cases we observed clusters of LSUs in the inclusions of double-membraned granules described earlier (Fig. [4]F, Fig. [5]D,E). It is, in principle, possible that these targets are situated above or below the imaged granules, since the granule positions in z cannot be determined using 2D projections. However, in the case of Fig. [5]E, the detected LSUs span the whole lamella in the z direction (Fig. [5]F), while positions above or below a granule would result in LSUs situated exlusively at the top or bottom of the lamella. This is consistent with the earlier hypothesis that the inclusions are of cytoplasmic origin.

Does DeCo-LACE induce aberrations that affect 2DTM?

Within the eight lamellae we found different numbers of detected targets, ranging from 1089 to 6433 per lamella (Fig. [6]A). Lamella$_{\mathrm{EUC}}$ 1 had the most detected targets, but also has the largest surface area and contained cytoplasm from two cells. Lamella$_{\mathrm{FFF}}$ 4 had the fewest detected targets, but this particular lamella was dominated by a circular section of the nucleus, with only small pockets of cytoplasm (Fig. [4 - figure supplement 4]). In an attempt to normalize for these differences in area containing cytoplasm, we compared the number of detected targets per tile in tiles that contained more than one target, which should exclude tiles with non-cytosolic content (Fig. [6]B). While this measure had less variability, there were still differences. Lamella$_{\mathrm{EUC}}$ 4 had not only the fewest targets, but also the lowest density, which could be due to this lamella being the thinnest, or due to it sectioning the cell in an area with a lower concentration of ribosomes. Lamella$_{\mathrm{FFF}}$ 3 had a substantially higher number of ribosomes per tile. Since all of these lamellae were made from a cell-line under identical conditions, this underscores the necessity to collect data from large numbers of lamellae to overcome the inherent variability. When comparing the distribution of scores between lamellae, we found them to be fairly comparable with median SNRs ranging from 8.7 to 9.7 (Fig. [6]C). Lamella$_{\mathrm{EUC}}$ 1 had slightly lower scores compared to the rest, potentially due to its large size and connected mechanical instability during imaging. Overall, we did not observe differences in the number or SNR of detected targets between eucentric or fringe-free illumination conditions that were bigger than the observed inter-lamella variability.

Since the SNR values of 2DTM are highly sensitive to image quality, we reasoned we could use them to verify that DeCo-LACE does not introduce a systematic loss of image quality. We considered non-parallel illumination introduced by the unusually condensed beam and uncharacterized aberrations near the beam periphery. When plotting the SNR values of detected targets in all eight lamellae as a function of their location in the tiles, we found uniformly high SNR values throughout the illuminated areas for both eucentric and fringe-free focus illumination, demonstrating that both illumination schemes are suitable for DeCo-LACE (Fig. [6]D).

We also wondered whether large image shifts would lead to aberrations due to astigmatism or beam tilt [16]. We reasoned that if that was the case the number of detected targets should be highest in the center of the lamella where the applied beam image-shift is 0. Instead, we observed that in both eucentric and fringe-free focus conditions more

targets were detected at the "back" edge of the lamella (Fig. [6]E]). This may be due to the center of the cell being predominantly occupied by the nucleus, despite its segmentation in neutrophil-like cells. The increase in matches at the "back" of the lamellae compared to the "front" can also be explained by the thickness gradient of the lamellae (Fig. [4 - figure supplement 2]B, Fig. [4]B, Fig. [5]B). In addition, aberrations would be expected to cause average 2DTM SNRs to be higher when beam-image shift values are small. Instead, we found that SNRs where on average the highest at the "front" edge of the lamellae, presumably due to the thinner sample. We therefore conclude that factors other that beam image-shift or beam condensation aberrations are limiting 2DTM SNRS, predominantly the thickness of the lamellae.

Computation is the bottleneck of visual proteomics

All lamellae described above were derived from a clonal cell line under identical condition and thinned with the same parameters. This means that the substantial variability of detected targets between the lamellae must be due to technical variability, including area, thickness, mechanical stability, and location of the section within the cell. We therefore predict that further studies that want to draw quantitative and statistically relevant conclusions about the number and location of molecules under different experimental conditions, will require collection of orders of magnitude more data than in this study to gain enough statistical power given this variability. The samples used were prepared in two 24 h sessions on a FIB/SEM instrument, and imaging was performed during another two 24h session on the TEM microscope. Inspections of the timestamps of the raw data files revealed that the milling time per lamella was ~30 minutes and TEM imaging was accomplished in ~10 seconds per tile or 90 minutes for a ~ 6x6 µm lamella. Processing of the data, however, took substantially longer. Specifically, 2DTM of all tiles took approximately one week per lamella on 32 Nvidia A6000 GPUs. Computation is therefore a bottleneck in our current workflow, and further optimizations of the algorithm may be necessary increase throughput. Alternatively, this bottleneck could be reduced by increasing the number of processing units.

Discussion

In this study we developed an approach to image entire cellular cross-section using cryo-EM at high enough resolution to allow for 2DTM detection of the LSU. The two main advantages compared to previous approaches are high throughput of imaging and biological context for detected molecules. The requirement to increase throughput in cryo-EM data collection of cellular samples has been recognized in the recent literature. Most approaches described so far are tailored towards tomography. Peck et al. [21] and Yang et al. [22] developed approaches to increase the FOV of tomogram data-collection by using a montaging technique. Peck et al. used a similar "condensed-beam" approach as described here. However, the montages are substantially smaller in scope, covering carbon film holes of 2 µm diameter. Bouvette et al. [23] and Eisenstein et al. [24] are using beam image-shift to collect tilt-series in multiple locations in parallel to increase throughput. However, none of these approaches provide the full coverage

of a cellular cross-section that can be achieved using DeCo-LACE.

We observed granules containing a vesicle of putative cytosolic origin. We speculate that upon degranulation, the process in which granules fuse with the plasma membrane, these vesicles would be released into the extracelullar space. The main types of extracellular vesicles of this size are exosomes, up to 100 nm large vesicles derived from fusion of multivesicular bodies with the plasma membrane, and microvesicles, which are derived from direct budding of the plasma membrane [25]. We suggest that granulocytes could release a third type of extracellular vesicle, granule-derived vesicles (GDV), into the extracellular space. 2DTM showed that a subset of GDVs can contain ribosomes (Fig. [4]F, Fig. [5]D,E). This could indicate that these vesicles are transporting translation-capable mRNAs, as has been described for exosomes [26]. Further studies will be necessary to confirm the existence of GDVs in granulocytes isolated from mammals and to understand their functional significance.

As mentioned in the results, we found a consistent shading artifact pattern in our montages, that we believe is the result of non-linear behavior of the K3 camera. Indeed, when we average images with a condensed beam taken over vacuum we found in both focus conditions a consistent background pattern with a brighter region on the periphery of the illuminated area (Fig [4 - figure supplement 3]). This might be caused by dynamic adjustment of the internal camera counting threshold which expects columns of the sensor to be evenly illuminated as is the case for SPA applications. Since the signal of this pattern has mainly low-resolution components it is unlikely to affect 2DTM. However, it highlights that the non-linear behavior of the camera has to be taken into account when imaging samples with strongly varying density and unusual illumination schemes.

We found that even though we used beam image-shift extensively (up to 7 um), we did not see substantially reduced 2DTM SNR values in tiles acquired at high beam image-shift compared to tiles acquired with low or no beam image-shift. This is in contrast to reports in single-particle analysis (SPA) [27] where the induced beam tilt substantially reduced the resolution if it was not corrected during processing. It is possible that 2DTM is less sensitive to beam-tilt aberrations, since the template is free of any aberration and only the image is distorted, while in SPA the beam tilt will affect both the images and the reconstructed template.

Since we observed substantial variation in LSU density within and between lamellae, visual proteomics studies that use cryo-EM to establish changes in molecular organization within cells will require orders of magnitude more data than used in this study. One milestone would be to image enough data to represent one cellular volume, which for a small eukaryotic cells requires imaging approximately 100 lamellae. While data collection throughput on the TEM is fundamentally limited by the exposure time, this amount of data could be collected within 12 hours by improving the data acquisition scheme to perform all necessary calculations in parallel with actual exposure of the camera. Sample preparation using a FIB/SEM is also currently a bottleneck, but preparation of large lamellae with multiple cellular cross-sections using methods like WAFFLE [28] might allow sufficient throughput. As stated in the results, at least for 2DTM computation will remain challenging and approximately 17,000 GPU hours would be

required for a 100 lamellae dataset.

Materials and Methods

Grid preparation

ER-HoxB8 cells were maintained in RPMI medium supplemented with 10% FBS, penicillin/streptomycin, SCF, and estrogen [10] at 37 °C and 5% CO2. 120 h prior to grid preparation, cells were washed twice in PBS and cultured in the same medium except without estrogen. Differentiation was verified by staining with Hoechst-dye and inspection of nuclear morphology. Cells were then counted and diluted to $1 \cdot 10^6$ cells/ml. Grids (either 200 mesh copper grids, with a sillicone-oxide and 2 µm holes with a 2 µm spacing or 200 mesh gold grids with a thin gold film and 2 µm holes in 2 µm spacing) were glow-discharged from both sides using a 15 mA for 45 s. 3.5 µl of cell suspension was added to grids on the thin-film side and grids were blotted from the back side using a GP2 cryoplunger (Leica, Wetzlar, Germany) for 8 s and rapidly plunged into liquid ethane at -185 °C.

FIB-milling

Grids were loaded into an Aquilos 2 FIB/SEM (Thermo Fisher, Waltham, MA) instrument with a stage cooled to -190 °C. Grids were sputter-coated with platinum for 15 s at 45 mA and then coated with a layer of platinum-precursor by opening the GIS-valve for 45 s. An overview of the grid was created by montaging SEM images and isolated cells at the center of gridsquares were selected for FIB-milling. Lamellae were generated automatically using the AutoTEM software (Thermo Fisher), with the following parameters:

- Milling angle: 20°
- Rough milling: 3.2 µm thickness, 0.5 nA current
- Medium milling: 1.8 µm thickness, 0.3 nA current, 1.0° overtilt
- Fine milling: 1.0 µm tchickness, 0.1 nA current, 0.5° overtilt
- Finer milling: 700 nm thickness, 0.1 nA curent, 0.2° overtilt
- Polish 1: 450 nm thickness, 50 pA current
- Polish 2: 200 nm thickness, 30 pA current

This resulted in 6-10 µm wide lamella with 150-250 nm thickness as determined by FIB-imaging of the lamella edges.

Data collection

Grids were loaded into a Titan Krios TEM (Thermo Fisher) operated at 300 keV and equipped with a BioQuantum energy filter (Gatan, Pleasanton, CA) and K3 camera (Gatan). The microscope was aligned using a cross-grating grid on the stage. Prior to each session, we carefully performed the "Image/Beam" calibration in nanoprobe. We set

the magnification to a pixel size of 1.76 Å and condensed the beam to ~ 900 nm diameter, resulting in the beam being completely visible on the camera. To establish fringe-free conditions, the "Fine eucentric" procedure of SerialEM [29] was used to move a square of the cross-grating grid to the eucentric position of the microscope. The effective defocus was then set to 2 µm, using the "autofocus" routine of SerialEM. The objective focus of the microscope was changed until no fringes were visible. The stage was then moved in Z until images had an apparent defocus of 2 µm. The difference in stage Z-position between the eucentric and fringe-free conditions was used to move other areas into fringe-free condition.

Low magnification montages were used to find lamellae and lamellae that were sufficiently thin and free of contamination were selected for automated data collection. Overview images of each lamella were taken at 2250x magnification (38 Å pixel size). The corners of the lamella in the overview image were manually annotated in SerialEM and translated into beam image-shift values using SerialEM's calibration. A hexagonal pattern of beam image-shift positions was calculated that covered the area between the four corners in a serpentine way, with a $\sqrt{3} \cdot 425$ nm horizontal spacing and $3/4 \cdot 850$ nm vertical spacing. Exposures were taken at each position with a 30 $e^-/Å^2$ total dose. After each exposure, the defocus was estimated using the ctffind function of SerialEM and the focus for the next exposure was corrected by the difference between the estimated focus and the desired defocus of 800 nm. Furthermore, after each exposure the deviation of the beam from the center of the camera was measured and corrected using the "CenterBeamFromImage" command of SerialEM.

After data collection, a 20 s exposure at 2250x magnification of the lamella at 200 µm defocus was taken for visualization purposes. A Python script implementing this procedure is available at https://github.com/jojoelfe/deco_lace_template_matching_manuscript.

DeCo-LACE data processing

An overview of the data analysis pipeline is shown in Fig. 7.

Pre-processing Motion-correction, dose weighting and other preprocessing as detailed below was performed using *cis*TEM [30]. To avoid influence of the beam-edge on motion-correction, only a quarter of the movie in the center of the camera was considered for calculation of the estimated motion. After movie frames were aligned and summed, a mask for the illuminated area was calculated by lowpass filtering the image with a 100 Å resolution cutoff, thresholding the image at 10% of the maximal value and then lowpass filtering the mask again with a 100 Å resolution cutoff to smooth the mask edges. This mask was then used to select dark areas in the image and fill the pixels with Gaussian noise, with the same mean and standard deviation as the illuminated area. A custom version of the unblur program [31] implementing this procedure is available at [link to decolace branch]. During motion correction images were resampled to a pixel size of 1.5 Å. The contrast-transfer function (CTF) was estimated using ctffind [32], searching between 0.2 and 2 µm defocus.

2DTM The search template was generated from the atomic model of the mouse LSU (PDB 6SWA, exluding the Epb1 subunit) using the cryo-EM simulator implemented in *cis*TEM [33]. The match_template program [9] was used to search for this template in the movie-aligned, exposure-filtered and masked images, using a 1.5° angular step in out-of-plane angles and a 1.0° angular step in-plane. 11 defocus planes in 20 nm steps centered around the ctffind-determined defocus were searched. Targets were defined as detected when their matches with the template produced peaks with a singal-to-noise ratio (SNR) above a threshold of 7.75, which was chosen based on the one-false-positive-per-tile criterion [7].

Montage assembly The coordinates of each tile i, $\mathbf{c}_i$ [2D Vector in pixels] were initialized using beam image-shift of the tile, $\mathbf{b}_i$ [2D Vector in µm], and the ISToCamera matrix **IC**, as calibrated by SerialEM:

$$\mathbf{c}_i = \mathbf{IC} \cdot \mathbf{b}_i$$

A list of tile pairs i, j that overlap were assembled by selecting images where $|\mathbf{c}_i - \mathbf{c}_j| < D_{Beam}$. In order to calculate the precise offset between tiles i and j, $\mathbf{r}_{i,j}$, we calculated the cross-correlation between the two tiles, masked to the overlapping illuminated area using the scikit-image package [34] was used to calculate refined offsets . The coordinates $\mathbf{c}_i$ were then refined by a least-square minimization against $\mathbf{r}_{i,j}$:

$$\min_{\mathbf{c}} \sum_{pairs} (\mathbf{r}_{i,j} - (\mathbf{c}_i - \mathbf{c}_j))^2$$

using the scipy package [35]. The masked cross-correlation and the least-square minimization was repeated once more to arrive at the final tile alignment.

The x,y coordinates of target n detected by 2DTM in the tile i, $\mathbf{m}^{\mathrm{T}}_{n,i}$, was transformed into the montage frame by adding the coordinate of the tile.

$$\mathbf{m}^{\mathrm{M}}_{n} = \mathbf{m}^{\mathrm{T}}_{n,i} + \mathbf{c}_i$$

The z coordinate of each target was calculated as the sum of the defocus offset for the target, the estimated defocus of the tile, and the nominal defocus of the microscope when the tile was acquired.

Images were rendered using UCSF ChimeraX [36] using a custom extension to render 2DTM results available at https://github.com/jojoelfe/tempest. The Python scripts used for data processing are available under https://github.com/jojoelfe/deco_lace_template_matching_manuscript.

Acknowledgments

The authors would like to thank Bronwyn Lucas, Carsten Sachse, and Chen Xu for helpful suggestions and careful reading of the manuscriptas as well as members of the Grigorieff lab for helpful discussions. Data was collected at the UMass Chan Medical School Cryo-EM core with help by Kankang Song, Christna Ouch, and Chen Xu.

Data availability

Cryo-EM movies, motion-corrected images and 2DTM results have been deposited in EMPIAR under accession code [will be inserted]. The custom cisTEM version is available under https://github.com/jojoelfe/cisTEM/tree/2574dbdf6161658fd177660b3a841100a792f61b until features have been integrated into a cisTEM release. The ChimeraX extension for rendering is available under https://github.com/jojoelfe/tempest. This manuscript was prepared using the manubot package [37] . The corresponding repository containing all scripts used for figure generation can be found under https://github.com/jojoelfe/deco_lace_template_matching_manuscript.

Conflicts of interest

The Authors declare that there is no conflict of interest.

Figures

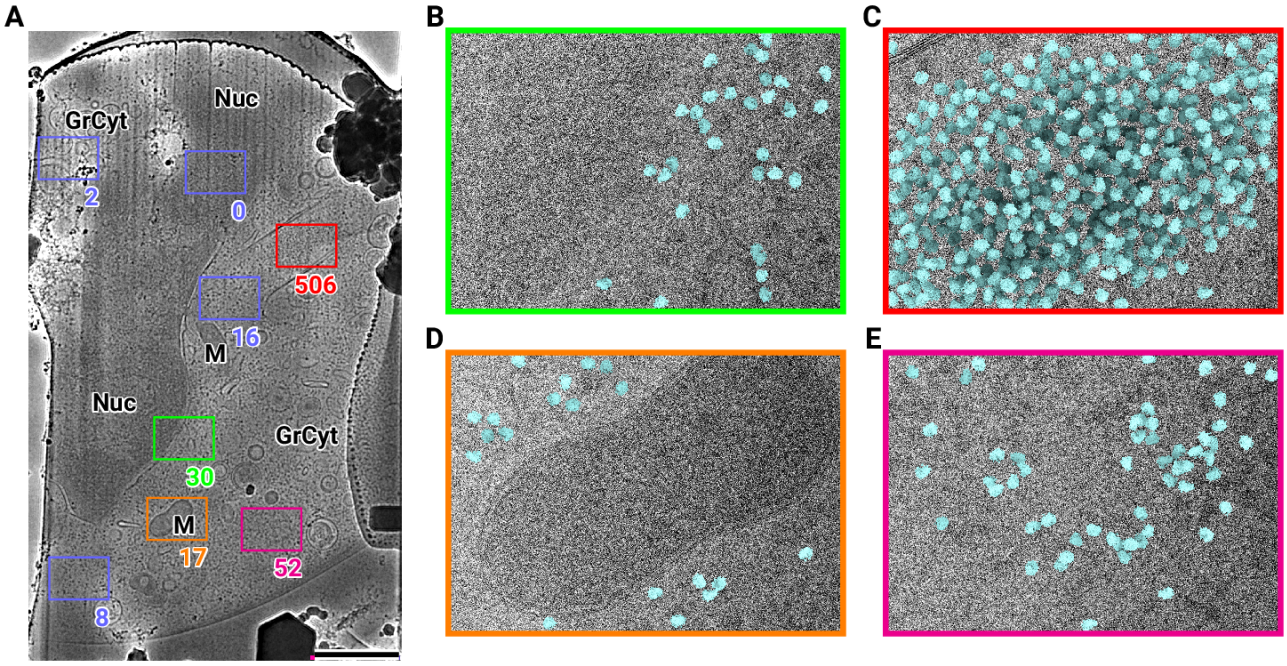

Figure 1: 2D template matching of the large subunit of the ribosome in fib-milled neutrophil-like cells (A) Overview image of the lamella. Major cellular regions are labeled, as Nucleus (Nuc), Mitochondria (M), and granular cytoplasm (GrCyt). FOVs where high-magnification images for template matching where acquired are indicated as boxes with the number of detected targets indicated on the bottom right. FOVs displayed in Panels B-E are color-coded. Scalebar corresponds to 1 µm. (B-E) FOVs with projection of detected LSUs shown in cyan. (B) Perinuclear region, the only detected targets are in the cytoplasmic half. (C) Cytoplasmic region with high density of ribosomes (D) Mitochondrium, as expected there are only detected LSUs in the cytoplasmic region (E) Cytoplasm, with low density of ribosomes.

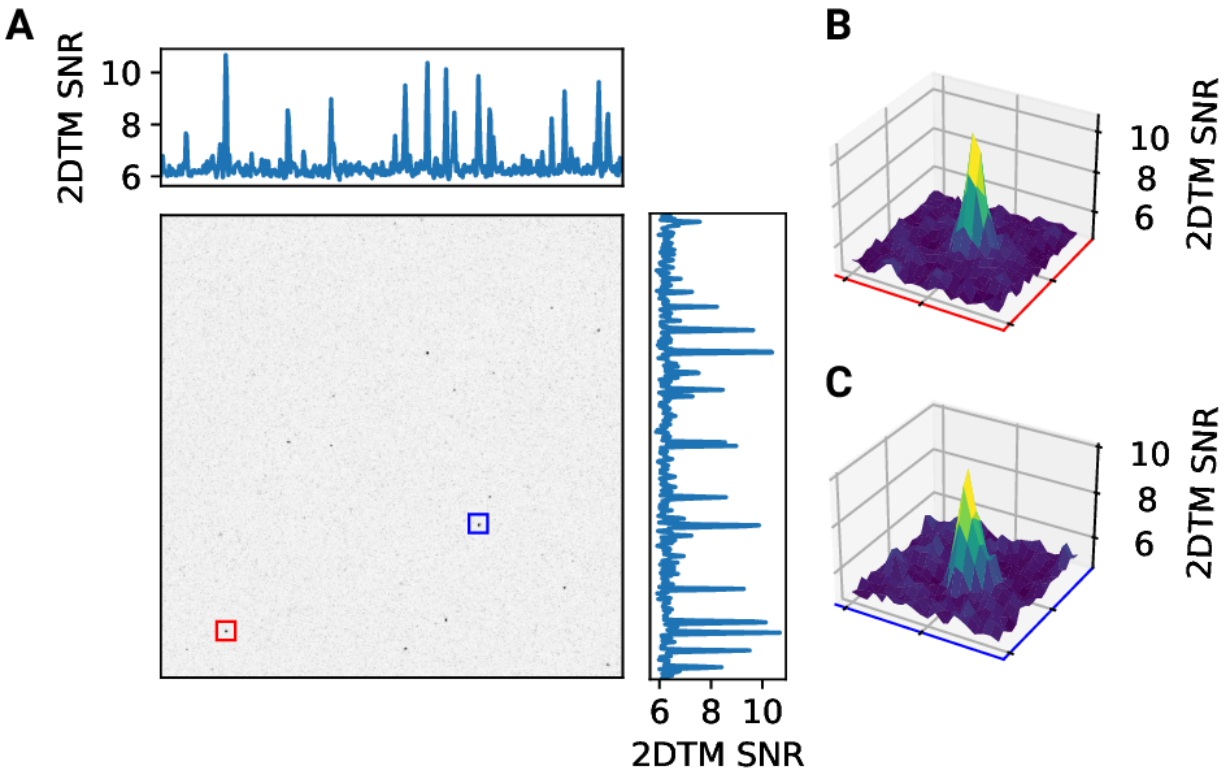

Figure 2 - figure supplement 1: 2D template matching of the large subunit of the ribosome in fib-milled neutrophil-like cells (A) Maximum intensity projection (MIP) cross-correlation map of micrograph shown in Figure 1 (B+C) 3D plot of MIP regions indicated by color boxes in Panel A

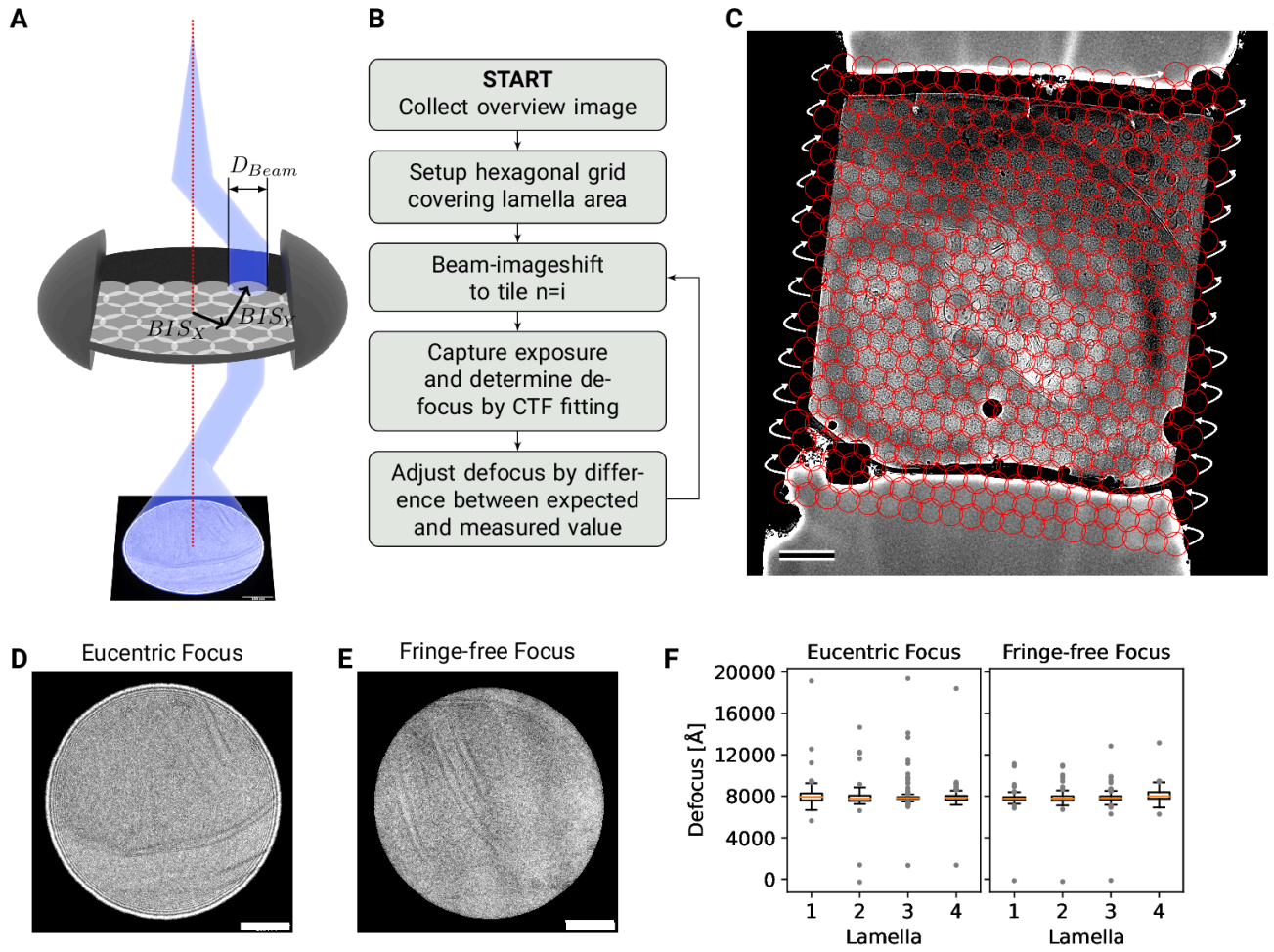

Figure 2: DeCo-LACE approach (A) Graphic demonstrating the data-collection strategy for DeCo-LACE. The electron beam is condensed to a diameter D_{Beam} that allows captured of the whole illuminated area on the camera. Beam-image shift along X and Y (BIS_X,BIS_Y) is used to scan the whole lamella (B) Diagram of the collection algorithm (C) Example overview image of a lamella with the designated acquisition positions and the used beam diameter indicated with red circles. Scalebar corresponds to 1 µm. (D+E) Representative micrographs takne with a condensed beam at eucentric focus (D) or fringe-free focus (E). Scalebar corresponds to 100 nm. (F) Boxplot of defocus measured by ctffind of micrographs taken by the DeCo-LACE approach on four lamellae images at eucentric focus and four lamellae imaged with fringe-free focus.

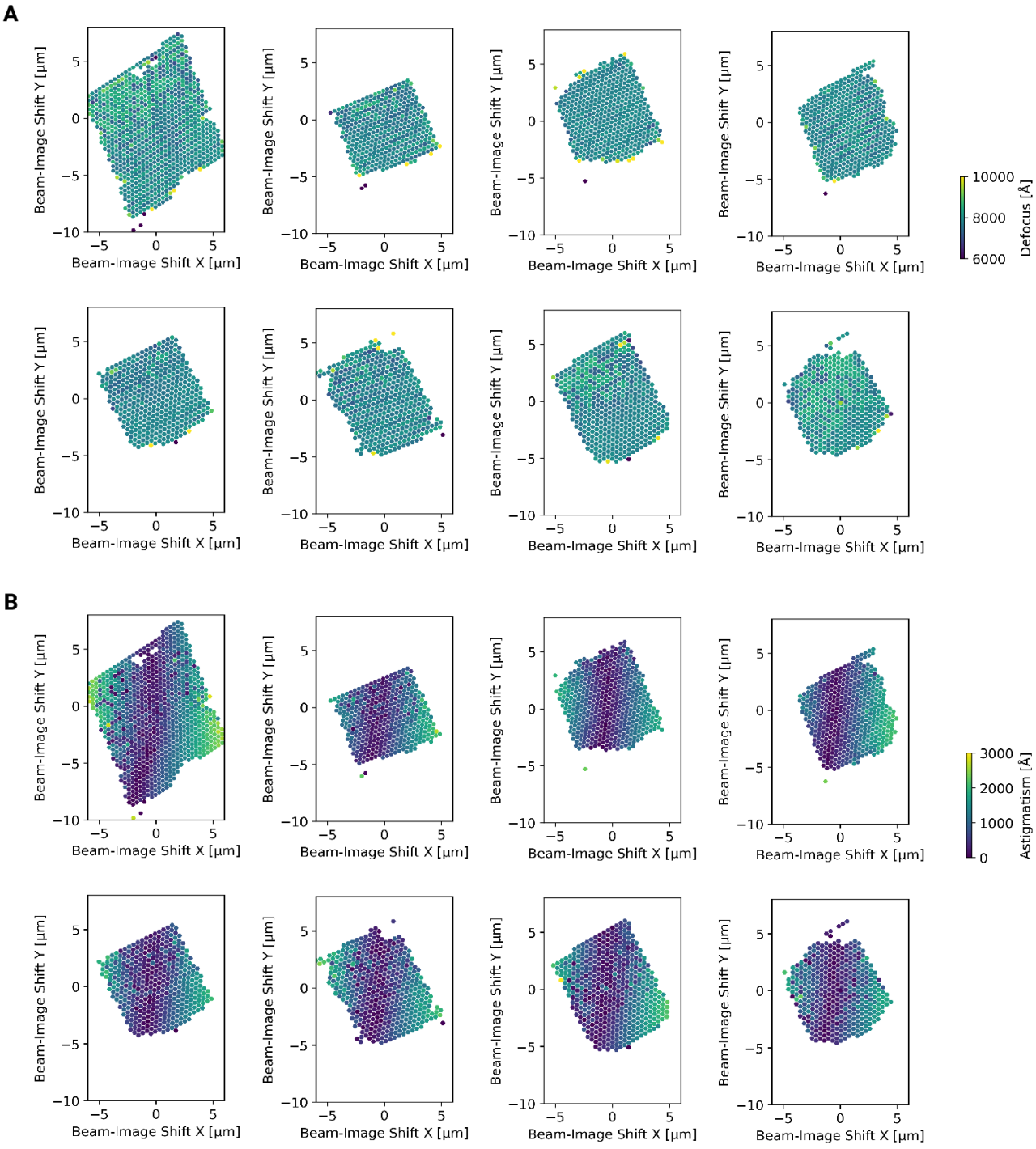

Figure 3 - figure supplement 1: Defocus estimation of individual tiles of DeCo-LACE montages (A) Defocus values of individual micrographs taken using the DeCo-LACE approach plotted as a function of the beam image-shift values. (B) Defocus astigmatism of individual micrographs taken using the DeCo-LACE approach plotted as a function of the beam image-shift values.

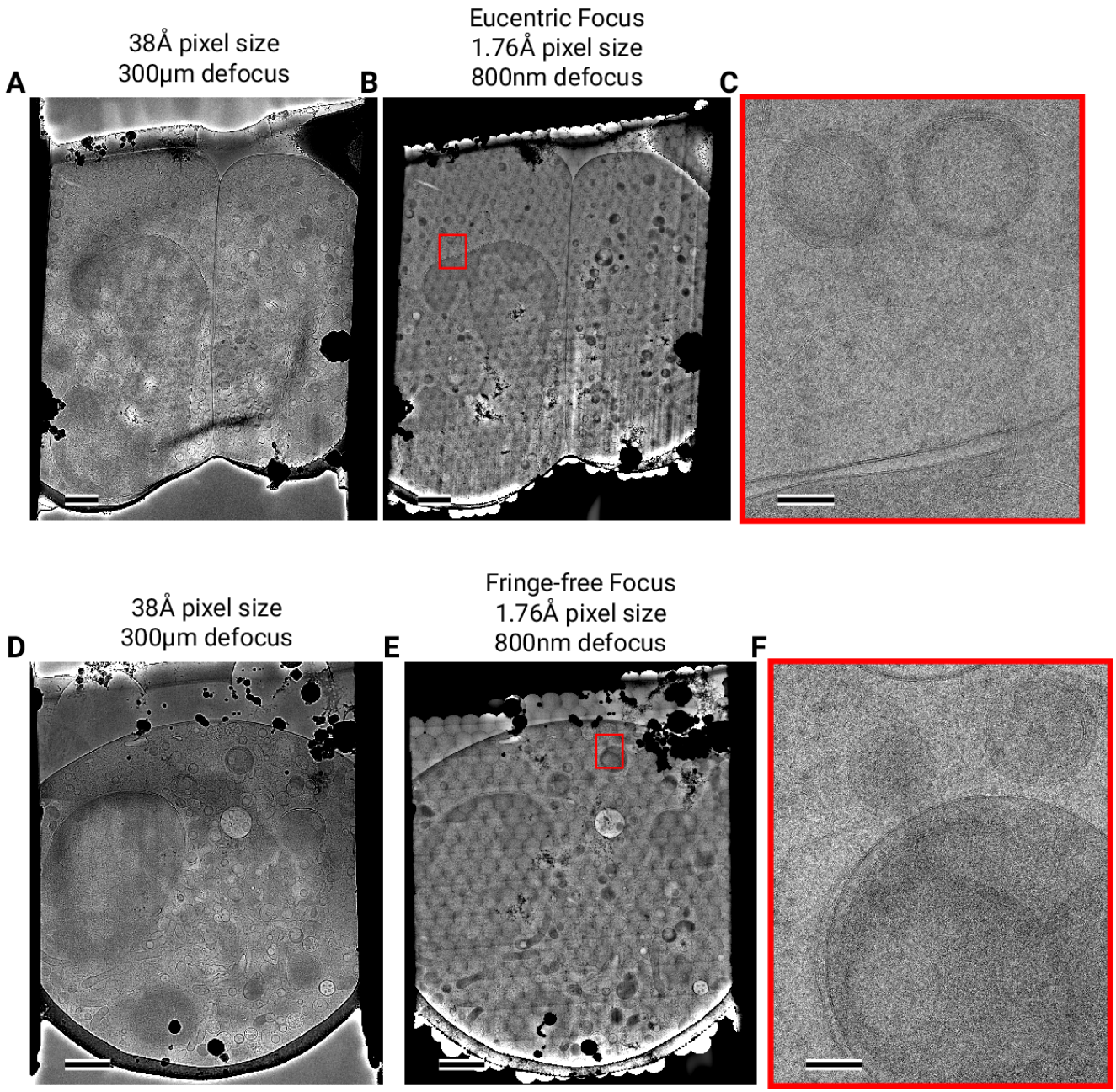

Figure 3: Assembling DeCo-LACE exposures into montages (A) Overview image of Lamella$_{EUC}$ 1 taken at low magnification. Scalebar corresponds to 1 µm. (B) Overview of Lamella$_{EUC}$ 1 created by montaging high magnification images taken with the DeCo-LACE approach. Scalebar corresponds to 1 µm. (C) Zoom-in into red box in panel B. Slight beam-fringe artifacts are visible. Scalebar corresponds to 100 nm. (D) Overview image of Lamella$_{FFF}$ 4 taken at low magnification. Scalebar corresponds to 1 µm. (E) Overview of Lamella$_{FFF}$ 4 created by montaging high magnification images taken with the DeCo-LACE approach. Scalebar corresponds to 1 µm. (F) Zoom-in into red box in panel E. No beam-fringe artifacts are visible. Scalebar corresponds to 100 nm.

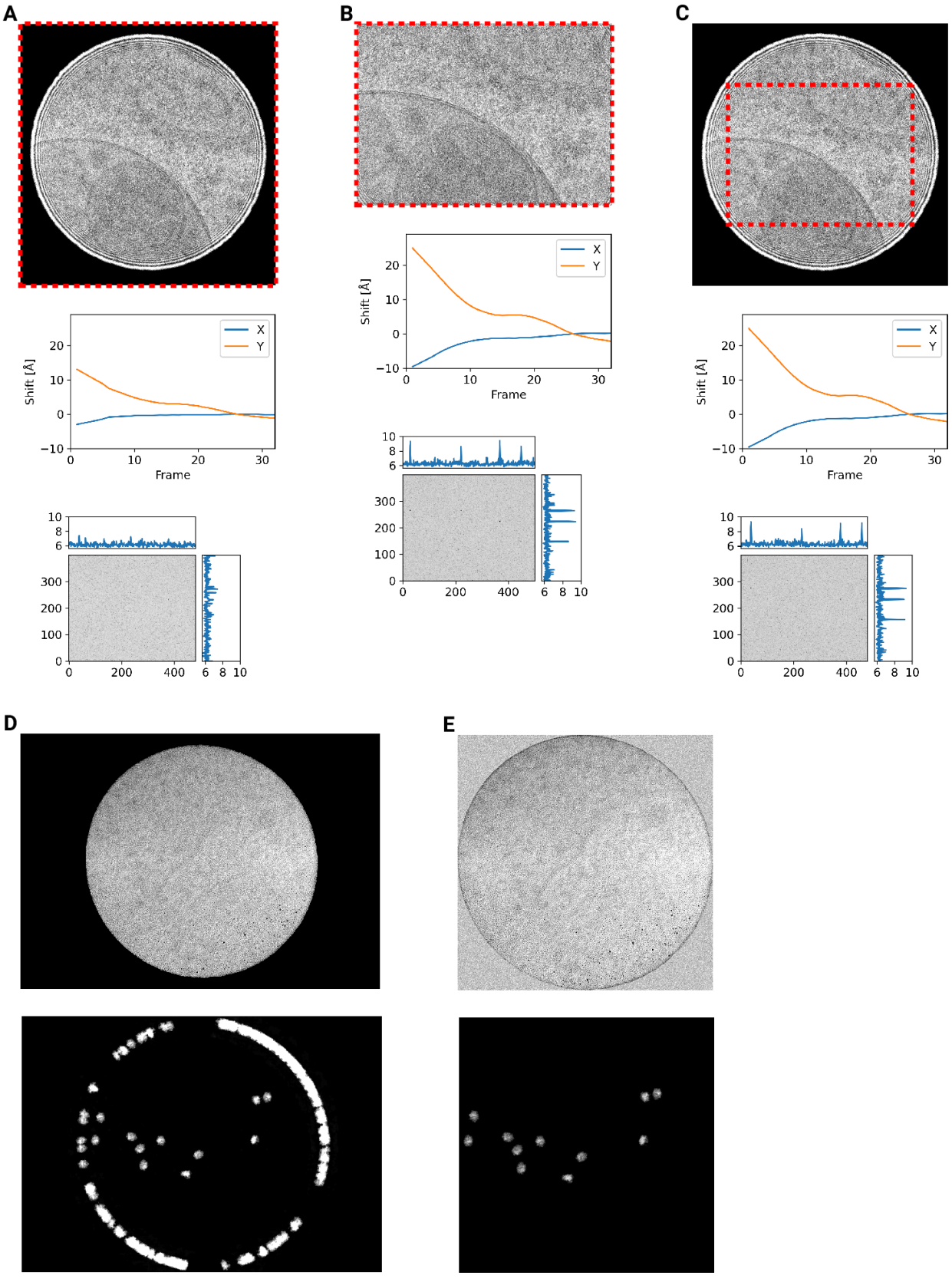

Figure 4 - figure supplement 1: Motion correction of movies with condensed beams. At the top of each panel is an average of the movie that was motion-corrected with a red dashed box indicating the region that was used to estimate shifts. Below is a graph indicating the estimated shifts of the individual frames of the movie. Below this is the MIP of 2DTM using the large subunit of the mouse ribosome. (A) Motion correction of the whole movie (B) Notion correction of a cropped region of the movie that eliminates the beam edges (C) Motion correction of the whole movie, using only the central region to estimate the shifts

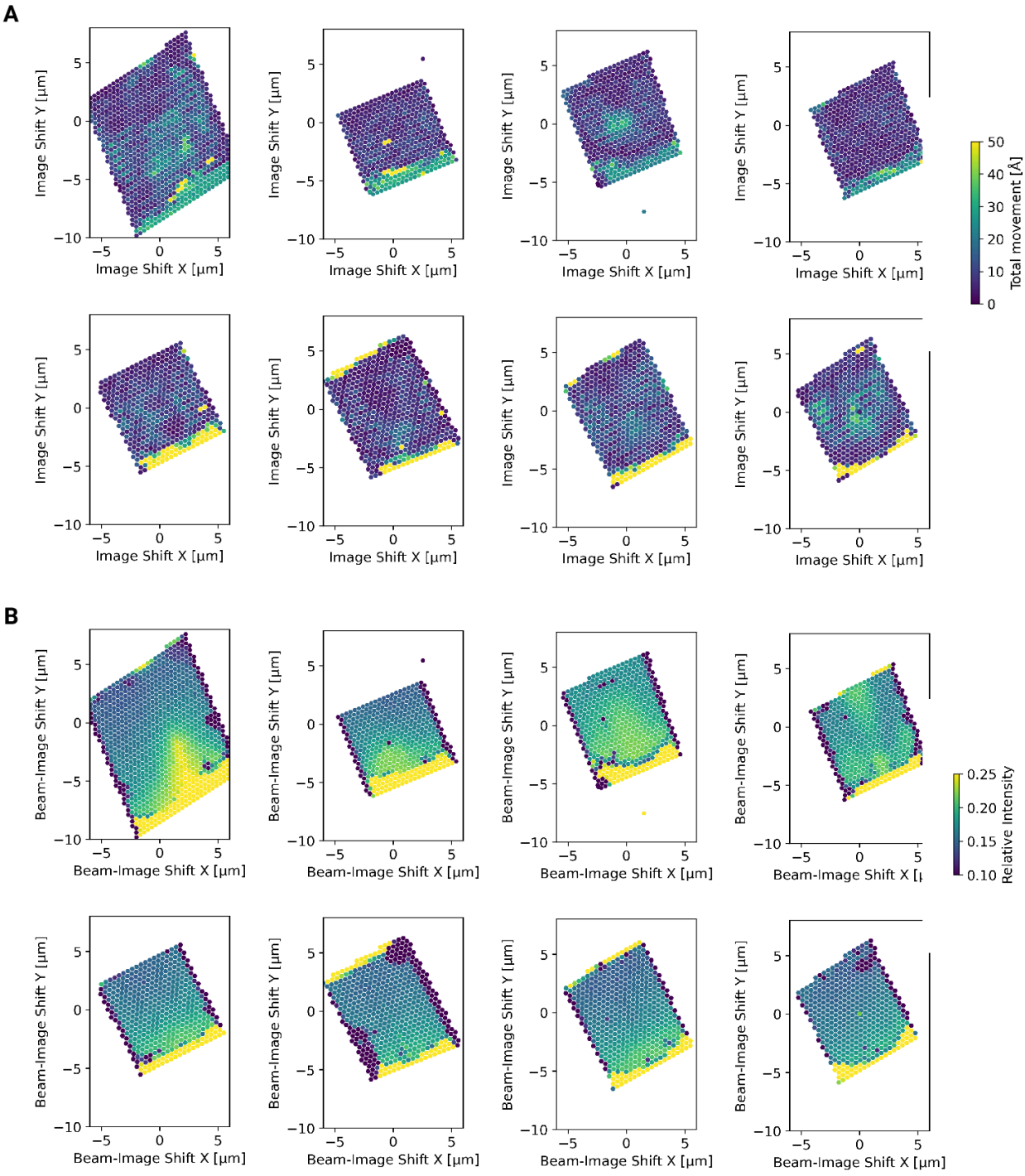

Figure 4 - figure supplement 2: Motion correction of individual tiles imaged using the DeCo-LACE approach (A) Total estimated motion of individual micrographs taken using the DeCo-LACE approach plotted as a function of the beam image-shift values. (B) Electron intensity of individual micrographs taken using the DeCo-LACE approach plotted as a function of the beam image-shift values.

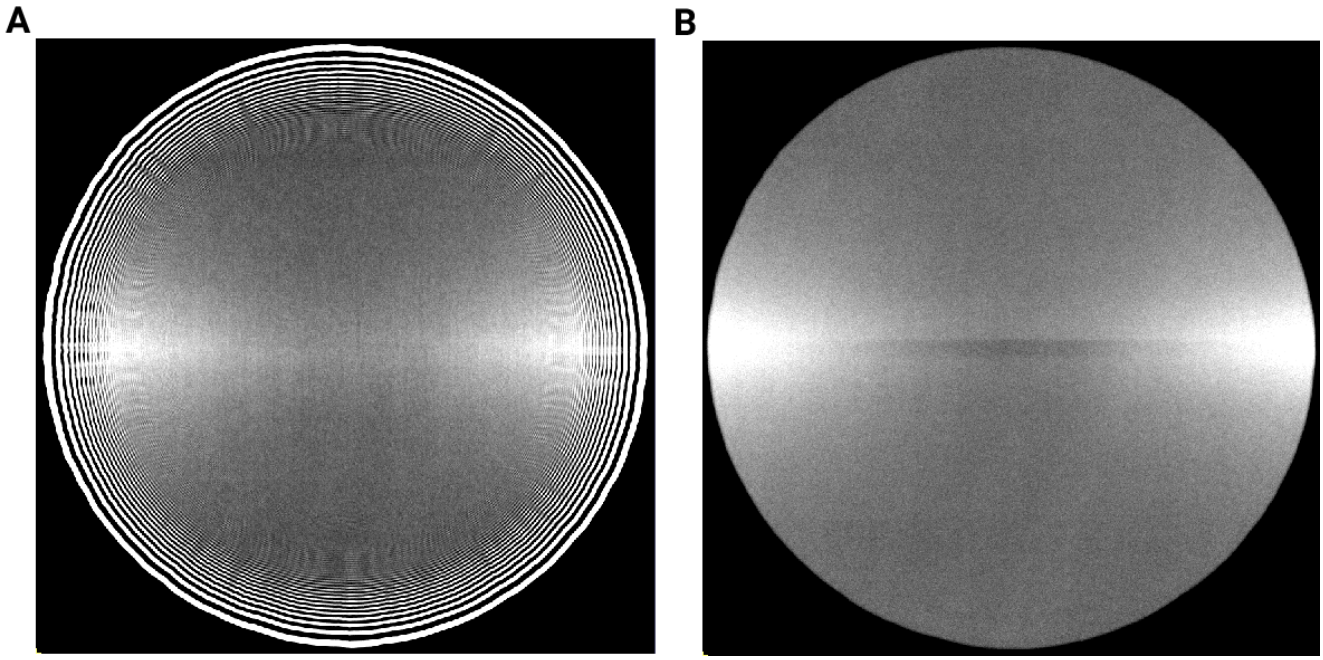

Figure 4 - figure supplement 3: Averages of micrographs taken with a condensed beam over vacuum using a Gatan K3 detector. Contrast and Brightness have been adjusted to highlight uneven dose response. (A) Eucentric Focus (B) Fringe-free Focus

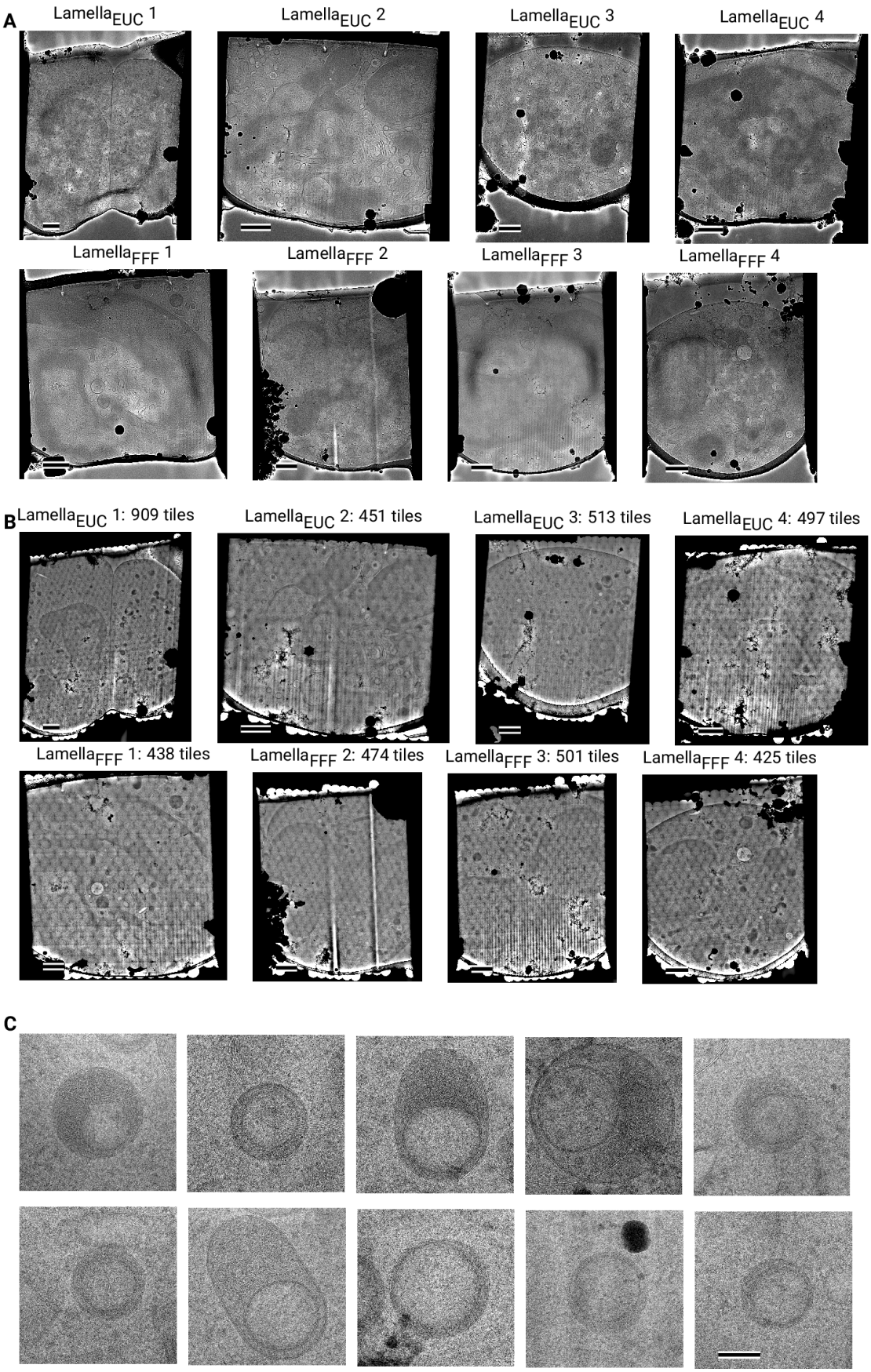

Figure 4 - figure supplement 4: Overview images of lamellae imaged using the DeCo-LACE approach taken at low-magnification (A) Overviews taken at low magnification. Scalebar corresponds to 1 µm. (B) Overviews assembled using the DeCo-LACE approach. Scalebar corresponds to 1 µm. (C) Representative examples of a class of granules containing a putatively cytosolic inclusion. Scalebar corresponds to 100 nm.

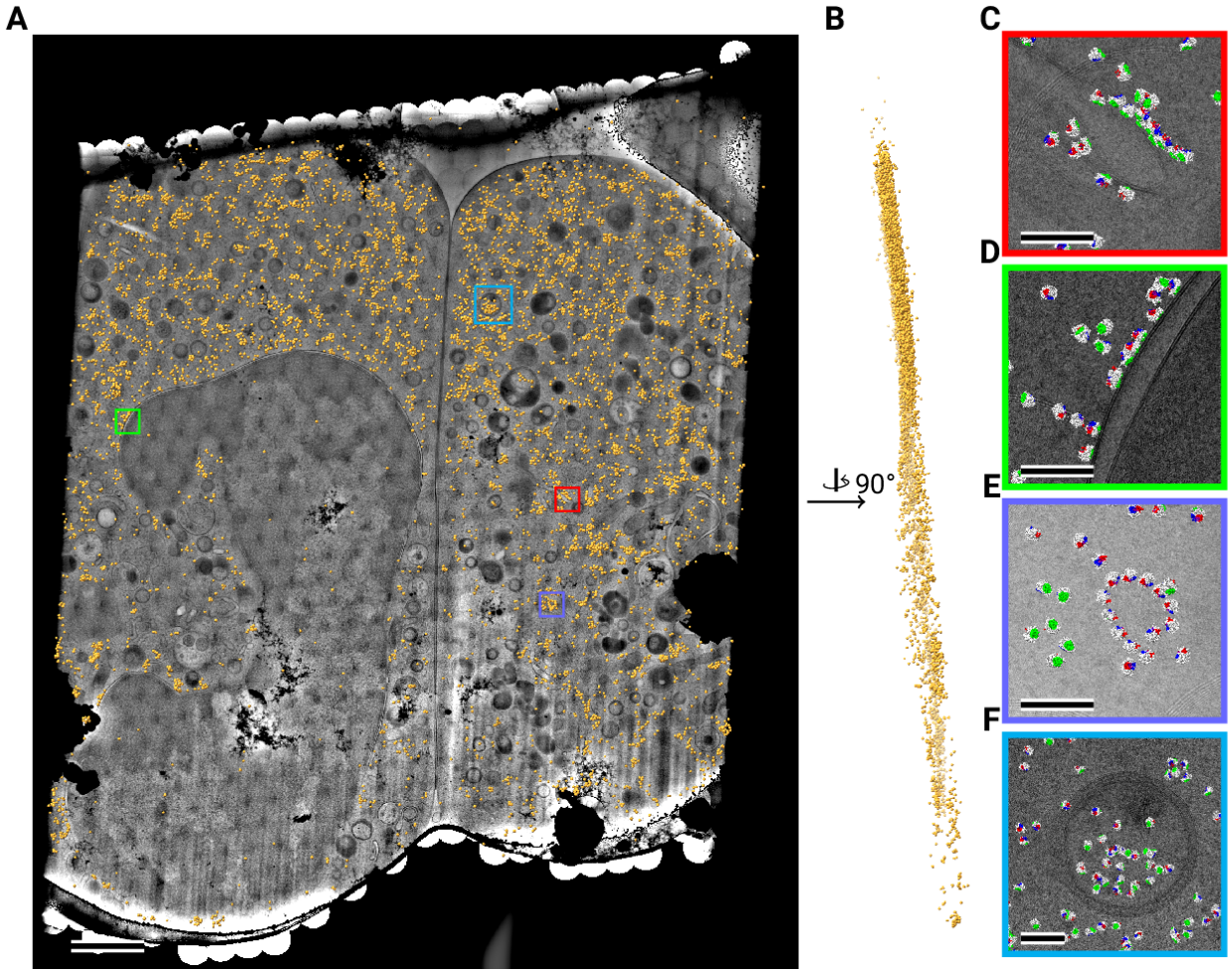

Figure 4: Template matching in lamella imaged using the DeCo-LACE approach at eucentric focus (A) Montage of Lamella$_{EUC}$ 1 overlaid with detected targets colored in orange. Scalebar corresponds to 1 µm. (B) Side view of detected targets in the lamella, such that the direction of the electron beam is horizontal. (C-F) Magnified area of panel A showing rough ER with associated ribosomes (C), outer nuclear membrane with associated ribosomes (D), ribsomes arranged in a circular fashion (E), ribosomes enclosed in a less electron dense inclusion in a granule (F). Ribosomes are colored in white with the surface of the peptide exit tunnel colored in green and the A, P, and E sites colored in blue, purple, and red, respectively.Scalebar corresponds to 100 nm.

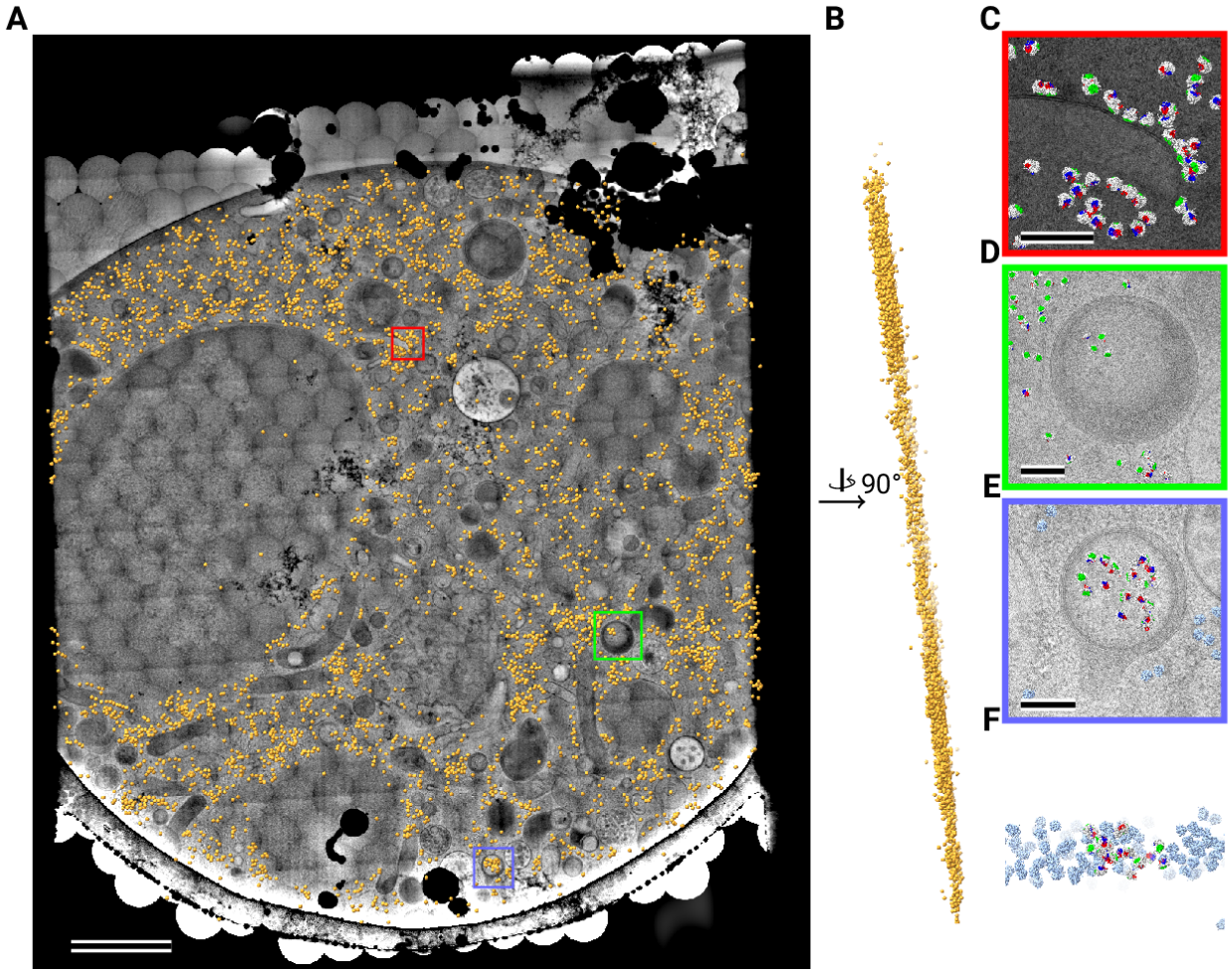

Figure 5: Template matching in lamella imaged using the DeCo-LACE approach at fringe-free focus (A) Montage of Lamella$_{FFF}$ 4 overlaid with detected targets colored in orange. Scalebar corresponds to 1 µm. (B) Side view of detected targets in the lamella, such that the direction of the electron beam is horizontal. (C-E) Magnified area of panel A showing rough ER with associated ribosomes (C) and ribosomes enclosed in a less electron dense inclusion in a granule (D,E). (F) Side view of panel E. Ribosomes are colored in white with the surface of the peptide exit tunnel colored in green and the A, P, and E sites colored in blue, purple, and red, respectively. Scalebar corresponds to 100 nm.

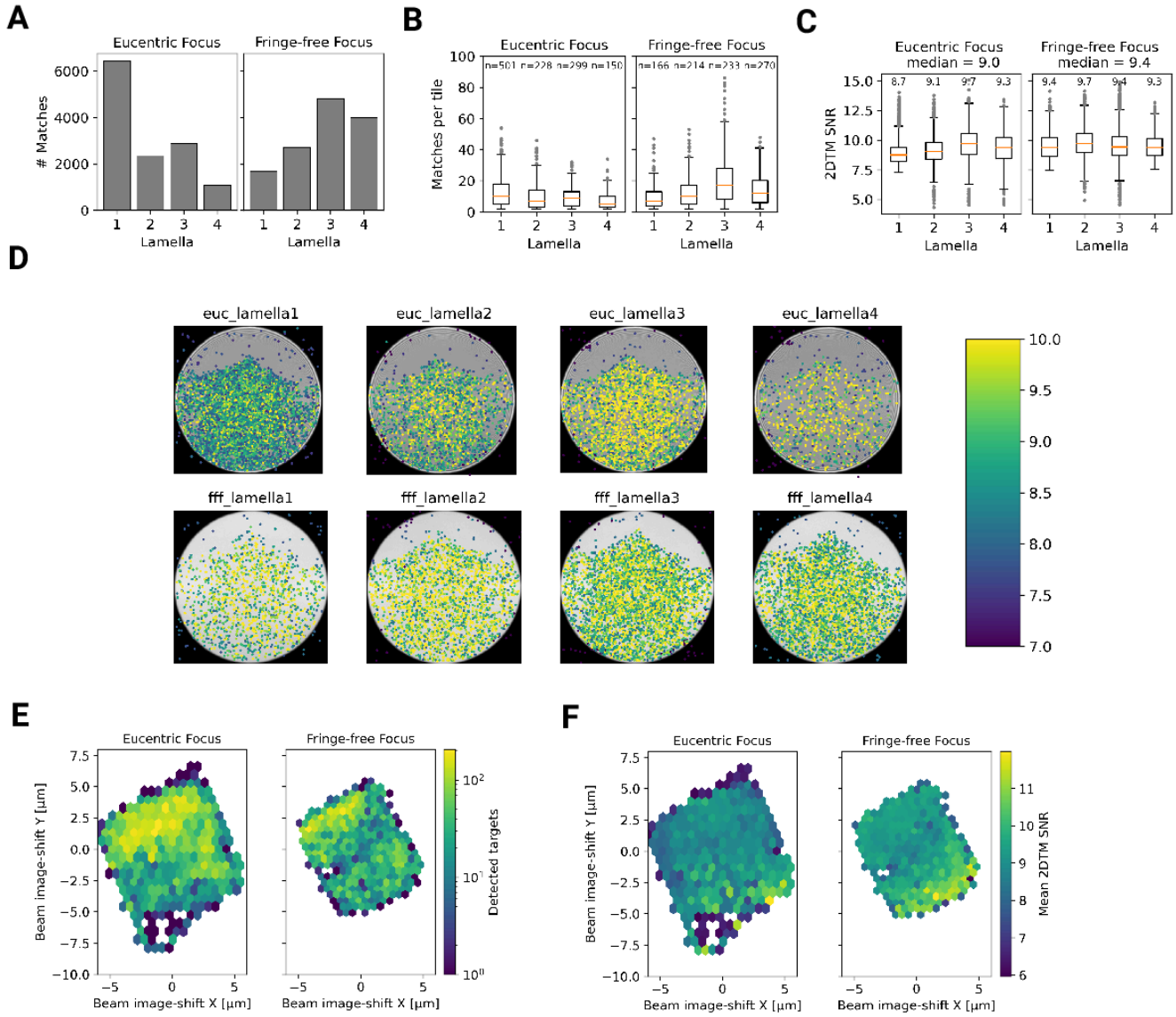

Figure 6: Statistics of 2DTM on lamella imaged using DeCo-LACE (A) Number of detected targets in each lamella (B) Distribution of targets per tile in each lamella. Only tiles with two or more detected targets were included (C) Distribution of SNRs in each lamella (D) For each lamella an average of all tiles is shown. Overlaid is a scatterplot of all detected targets in these tiles according to their in-tile coordinates. Scatterplot is colored according to the 2DTM SNR. There are no detected targets in the top circle-circle intersection due to radiation damage from previous exposures. (E) 2D histogram of number of detected targets as a function of beam-image shift (F) Mean 2DTM SNR as a function of beam-image shift

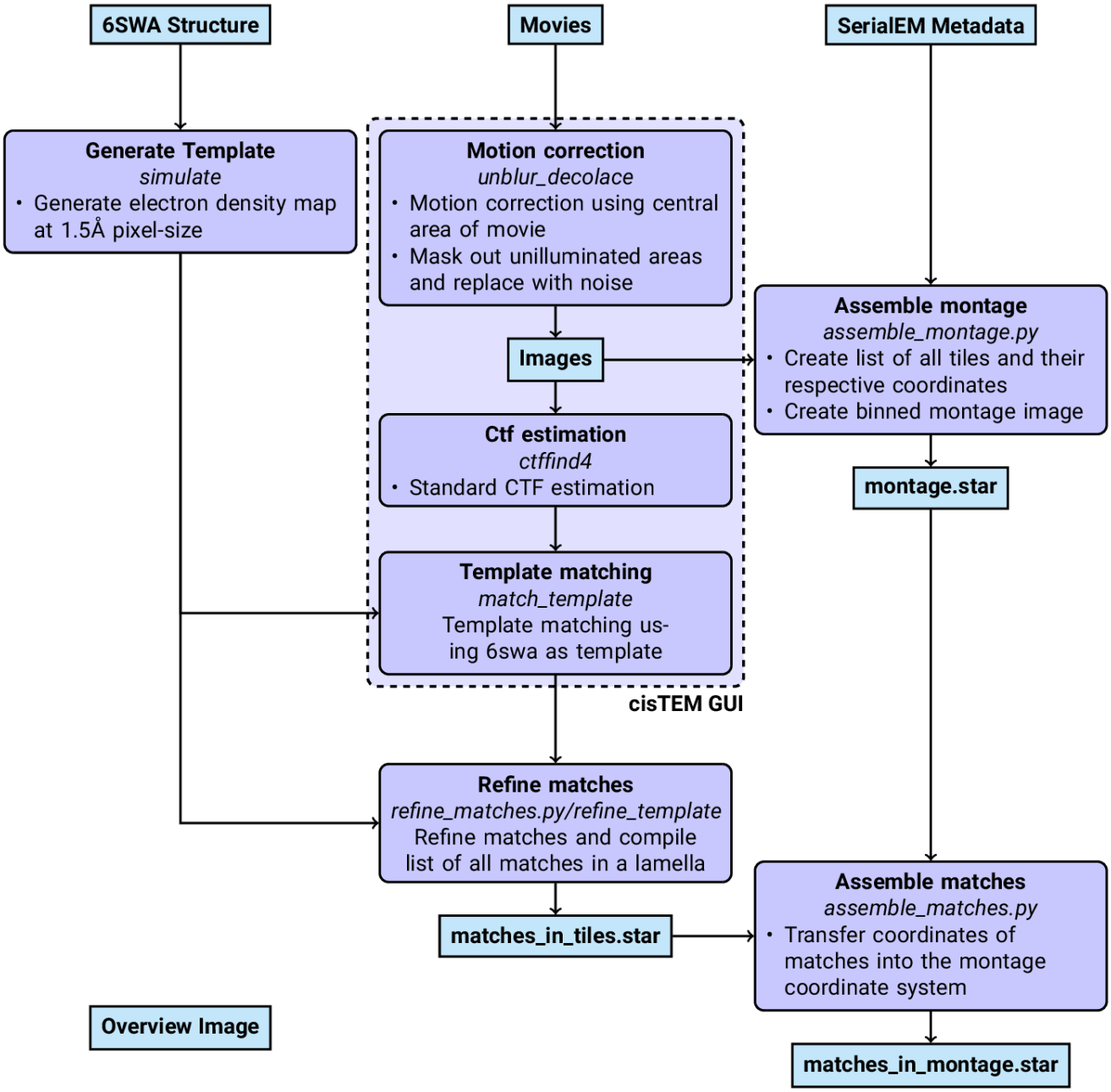

Figure 7: Workflow of DeCo-LACE processing

Figure Movie 1: Movie of detected LSU targets in Lamella$_{EUC}$ 1, corresponding to Figure 5

Figure Movie 2: Movie of detected LSU targets in Lamella$_{FFF}$ 4, corresponding to Figure 6

References

381 1. **Label-free, normalized quantification of complex mass spectrometry data for proteomic analysis** Noelle M Griffin, Jingyi Yu, Fred Long, Phil Oh, Sabrina Shore, Yan Li, Jim A Koziol, Jan E Schnitzer
Nature Biotechnology (2010-01) https://doi.org/fshgnc DOI: 10.1038/nbt.1592 · PMID: 20010810 · PMCID: PMC2805705

382

383 2. **Fluorescence microscopy** Jeff W Lichtman, José-Angel Conchello
Nature Methods (2005-11-18) https://doi.org/bbpg4n DOI: 10.1038/nmeth817 · PMID: 16299476

384

385 3. **A visual approach to proteomics** Stephan Nickell, Christine Kofler, Andrew P Leis, Wolfgang Baumeister
Nature Reviews Molecular Cell Biology (2006-02-15) https://doi.org/d6d5mq DOI: 10.1038/nrm1861 · PMID: 16482091

386

387 4. **Electron microscopy of frozen hydrated sections of vitreous ice and vitrified biological samples** AW McDowall, J-J Chang, R Freeman, J Lepault, CA Walter, J Dubochet
Journal of Microscopy (1983-07) https://doi.org/bdnzmv DOI: 10.1111/j.1365-2818.1983.tb04225.x · PMID: 6350598

388

389 5. **Opening windows into the cell: focused-ion-beam milling for cryo-electron tomography** Elizabeth Villa, Miroslava Schaffer, Jürgen M Plitzko, Wolfgang Baumeister
Current Opinion in Structural Biology (2013-10) https://doi.org/f537jp DOI: 10.1016/j.sbi.2013.08.006 · PMID: 24090931

390

391 6. **Electron tomography of cells** Lu Gan, Grant J Jensen
Quarterly Reviews of Biophysics (2011-11-15) https://doi.org/czj9hr DOI: 10.1017/s0033583511000102 · PMID: 22082691

392

393 7. **Single-protein detection in crowded molecular environments in cryo-EM images** JPeter Rickgauer, Nikolaus Grigorieff, Winfried Denk
eLife (2017-05-03) https://doi.org/gnq4q4 DOI: 10.7554/elife.25648 · PMID: 28467302 · PMCID: PMC5453696

394

395 8. **Label-free single-instance protein detection in vitrified cells** JPeter Rickgauer, Heejun Choi, Jennifer Lippincott-Schwartz, Winfried Denk
Cold Spring Harbor Laboratory (2020-04-24) https://doi.org/gpbjfd DOI: 10.1101/2020.04.22.053868

396

9. **Locating macromolecular assemblies in cells by 2D template matching with cisTEM** Bronwyn A Lucas, Benjamin A Himes, Liang Xue, Timothy Grant, Julia Mahamid, Nikolaus Grigorieff
eLife (2021-06-11) https://doi.org/gkkc49 DOI: 10.7554/elife.68946 · PMID: 34114559 · PMCID: PMC8219381

10. **Inhibition of Dihydroorotate Dehydrogenase Overcomes Differentiation Blockade in Acute Myeloid Leukemia** David B Sykes, Youmna S Kfoury, François E Mercier, Mathias J Wawer, Jason M Law, Mark K Haynes, Timothy A Lewis, Amir Schajnovitz, Esha Jain, Dongjun Lee, ... David T Scadden
Cell (2016-09) https://doi.org/f3r5jr DOI: 10.1016/j.cell.2016.08.057 · PMID: 27641501 · PMCID: PMC7360335

11. **Hallmarks of ribosomopathies** Kim R Kampen, Sergey O Sulima, Stijn Vereecke, Kim De Keersmaecker
Nucleic Acids Research (2019-07-27) https://doi.org/gpbjfm DOI: 10.1093/nar/gkz637 · PMID: 31350888 · PMCID: PMC7026650

12. **Diagnostic and prognostic implications of ribosomal protein transcript expression patterns in human cancers** James M Dolezal, Arie P Dash, Edward V Prochownik
BMC Cancer (2018-03-12) https://doi.org/gc87j9 DOI: 10.1186/s12885-018-4178-z · PMID: 29530001 · PMCID: PMC5848553

13. **In situ single particle classification reveals distinct 60S maturation intermediates in cells** Bronwyn A Lucas, Kexin Zhang, Sarah Loerch, Nikolaus Grigorieff
Cold Spring Harbor Laboratory (2022-04-10) https://doi.org/gp4qrx DOI: 10.1101/2022.04.10.487797

14. **Protein Synthesis in the Developing Neocortex at Near-Atomic Resolution Reveals Ebp1-Mediated Neuronal Proteostasis at the 60S Tunnel Exit** Matthew L Kraushar, Ferdinand Krupp, Dermot Harnett, Paul Turko, Mateusz C Ambrozkiewicz, Thiemo Sprink, Koshi Imami, Manuel Günnigmann, Ulrike Zinnall, Carlos H Vieira-Vieira, ... Christian MT Spahn
Molecular Cell (2021-01) https://doi.org/gh7d72 DOI: 10.1016/j.molcel.2020.11.037 · PMID: 33357414 · PMCID: PMC8163098

15. **Advances in Single Particle Analysis Data Acquisition** Stan Konings, Maarten Kuijper, Jeroen Keizer, Fanis Grollios, Tjerk Spanjer, Peter Tiemeijer
Microscopy and Microanalysis (2019-08) https://doi.org/gp9bqm DOI: 10.1017/s1431927619005798

411 16. **High-quality, high-throughput cryo-electron microscopy data collection via beam tilt and astigmatism-free beam-image shift** Chunling Wu, Xiaojun Huang, Jing Cheng, Dongjie Zhu, Xinzheng Zhang
Journal of Structural Biology (2019-12) https://doi.org/gp2nq9 DOI: 10.1016/j.jsb.2019.09.013 · PMID: 31562921

412

413 17. **THE DEVELOPMENT OF NEUTROPHILIC POLYMORPHONUCLEAR LEUKOCYTES IN HUMAN BONE MARROW** Dorothy Ford Bainton, Joan L Ullyot, Marilyn G Farquhar
Journal of Experimental Medicine (1971-10-01) https://doi.org/chkbcm DOI: 10.1084/jem.134.4.907 · PMID: 4106490 · PMCID: PMC2138991

414

415 18. **Routine determination of ice thickness for cryo-EM grids** William J Rice, Anchi Cheng, Alex J Noble, Edward T Eng, Laura Y Kim, Bridget Carragher, Clinton S Potter
Journal of Structural Biology (2018-10) https://doi.org/gfbpj2 DOI: 10.1016/j.jsb.2018.06.007 · PMID: 29981485 · PMCID: PMC6119488

416

417 19. **Optimized cryo-focused ion beam sample preparation aimed at in situ structural studies of membrane proteins** Miroslava Schaffer, Julia Mahamid, Benjamin D Engel, Tim Laugks, Wolfgang Baumeister, Jürgen M Plitzko
Journal of Structural Biology (2017-02) https://doi.org/f9qfr6 DOI: 10.1016/j.jsb.2016.07.010 · PMID: 27444390

418

419 20. **Circularization of mRNA by eukaryotic translation initiation factors.** SE Wells, PE Hillner, RD Vale, AB Sachs
Molecular cell (1998-07) https://www.ncbi.nlm.nih.gov/pubmed/9702200 DOI: 10.1016/s1097-2765(00)80122-7 · PMID: 9702200

420

421 21. **Montage electron tomography of vitrified specimens** Ariana Peck, Stephen D Carter, Huanghao Mai, Songye Chen, Alister Burt, Grant J Jensen
Journal of Structural Biology (2022-06) https://doi.org/gp4qrs DOI: 10.1016/j.jsb.2022.107860 · PMID: 35487464

422

22. **Correlative cryogenic montage electron tomography for comprehensive in-situ whole-cell structural studies** Jie E Yang, Matthew R Larson, Bryan S Sibert, Joseph Y Kim, Daniel Parrell, Juan C Sanchez, Victoria Pappas, Anil Kumar, Kai Cai, Keith Thompson, Elizabeth R Wright
Cold Spring Harbor Laboratory (2022-01-02) https://doi.org/gp4qrv DOI: 10.1101/2021.12.31.474669

23. **Beam image-shift accelerated data acquisition for near-atomic resolution single-particle cryo-electron tomography** Jonathan Bouvette, Hsuan-Fu Liu, Xiaochen Du, Ye Zhou, Andrew P Sikkema, Juliana da Fonseca Rezende e Mello, Bradley P Klemm, Rick Huang, Roel M Schaaper, Mario J Borgnia, Alberto Bartesaghi
Nature Communications (2021-03-30) https://doi.org/gjphkb DOI: 10.1038/s41467-021-22251-8 · PMID: 33785757 · PMCID: PMC8009872

24. **Parallel cryo electron tomography on in situ lamellae** Fabian Eisenstein, Haruaki Yanagisawa, Hiroka Kashihara, Masahide Kikkawa, Sachiko Tsukita, Radostin Danev
Cold Spring Harbor Laboratory (2022-04-08) https://doi.org/gp4qrw DOI: 10.1101/2022.04.07.487557

25. **Shedding light on the cell biology of extracellular vesicles** Guillaume van Niel, Gisela D'Angelo, Graça Raposo
Nature Reviews Molecular Cell Biology (2018-01-17) https://doi.org/gct4df DOI: 10.1038/nrm.2017.125 · PMID: 29339798

26. **Exosome-mediated transfer of mRNAs and microRNAs is a novel mechanism of genetic exchange between cells** Hadi Valadi, Karin Ekström, Apostolos Bossios, Margareta Sjöstrand, James J Lee, Jan O Lötvall
Nature Cell Biology (2007-05-07) https://doi.org/d5df4s DOI: 10.1038/ncb1596 · PMID: 17486113

27. **High-resolution cryo-EM using beam-image shift at 200 keV** Jennifer N Cash, Sarah Kearns, Yilai Li, Michael A Cianfrocco
IUCrJ (2020-10-29) https://doi.org/gjwcfq DOI: 10.1107/s2052252520013482 · PMID: 33209328 · PMCID: PMC7642776

28. **Waffle Method: A general and flexible approach for improving throughput in FIB-milling** Kotaro Kelley, Ashleigh M Raczkowski, Oleg Klykov, Pattana Jaroenlak, Daija Bobe, Mykhailo Kopylov, Edward T Eng, Gira Bhabha, Clinton S Potter, Bridget Carragher, Alex J Noble
Nature Communications (2022-04-06) https://doi.org/gp4qrt DOI: 10.1038/s41467-022-29501-3 · PMID: 35387991 · PMCID: PMC8987090

29. **Automated electron microscope tomography using robust prediction of specimen movements** David N Mastronarde
Journal of Structural Biology (2005-10) https://doi.org/ff7gzx DOI: 10.1016/j.jsb.2005.07.007 · PMID: 16182563

30. **cisTEM, user-friendly software for single-particle image processing** Timothy Grant, Alexis Rohou, Nikolaus Grigorieff
eLife (2018-03-07) https://doi.org/gf5cq7 DOI: 10.7554/elife.35383 · PMID: 29513216 · PMCID: PMC5854467

31. **Measuring the optimal exposure for single particle cryo-EM using a 2.6 Å reconstruction of rotavirus VP6** Timothy Grant, Nikolaus Grigorieff
eLife (2015-05-29) https://doi.org/gf5cm7 DOI: 10.7554/elife.06980 · PMID: 26023829 · PMCID: PMC4471936

32. **CTFFIND4: Fast and accurate defocus estimation from electron micrographs** Alexis Rohou, Nikolaus Grigorieff
Journal of Structural Biology (2015-11) https://doi.org/f7xzgv DOI: 10.1016/j.jsb.2015.08.008 · PMID: 26278980 · PMCID: PMC6760662

33. **Cryo-TEM simulations of amorphous radiation-sensitive samples using multislice wave propagation** Benjamin Himes, Nikolaus Grigorieff
IUCrJ (2021-09-30) https://doi.org/gpzs9r DOI: 10.1107/s2052252521008538 · PMID: 34804546 · PMCID: PMC8562658

34. **scikit-image: image processing in Python** Stéfan van der Walt, Johannes L Schönberger, Juan Nunez-Iglesias, François Boulogne, Joshua D Warner, Neil Yager, Emmanuelle Gouillart, Tony Yu
PeerJ (2014-06-19) https://doi.org/gftp3s DOI: 10.7717/peerj.453 · PMID: 25024921 · PMCID: PMC4081273

449 35. **SciPy 1.0: fundamental algorithms for scientific computing in Python** Pauli Virtanen, Ralf Gommers, Travis E Oliphant, Matt Haberland, Tyler Reddy, David Cournapeau, Evgeni Burovski, Pearu Peterson, Warren Weckesser, Jonathan Bright, ...

Nature Methods (2020-02-03) https://doi.org/ggj45f DOI: 10.1038/s41592-019-0686-2 · PMID: 32015543 · PMCID: PMC7056644

450

451 36. **<scp>UCSF ChimeraX</scp> : Structure visualization for researchers, educators, and developers** Eric F Pettersen, Thomas D Goddard, Conrad C Huang, Elaine C Meng, Gregory S Couch, Tristan I Croll, John H Morris, Thomas E Ferrin

Protein Science (2020-10-22) https://doi.org/ghr6mn DOI: 10.1002/pro.3943 · PMID: 32881101 · PMCID: PMC7737788

452

453 37. **Open collaborative writing with Manubot** Daniel S Himmelstein, Vincent Rubinetti, David R Slochower, Dongbo Hu, Venkat S Malladi, Casey S Greene, Anthony Gitter

PLOS Computational Biology (2019-06-24) https://doi.org/c7np DOI: 10.1371/journal.pcbi.1007128 · PMID: 31233491 · PMCID: PMC6611653

454